CEA DAPNIA-04-278

Developments in the ray-tracing code Zgoubi for 6-D multiturn tracking in FFAG rings

F. Lemuet[*] and **F. Méot**[†]

November 29, 2004

Abstract

A geometrical method for 3-D modeling of the magnetic field in scaling and non-scaling FFAG magnets has been installed in the ray-tracing code Zgoubi. The method in particular allows a good simulation of field fall-offs and of merging fields in configurations of neighboring large magnets, while using realistic models of magnetic fields. That yields an efficient tool for lattice design and optimizations, and for 6-D tracking studies. It is applied for illustration to the simulation of an acceleration cycle in a 150 MeV radial sector proton FFAG.

[*]CERN AB, Geneva
[†]CEA DAPNIA, Saclay

Contents

1 Introduction **3**

2 The ray-tracing method, ingredients **3**

3 An N-uplet magnet procedure. FFAG magnet **4**
3.1 Field fall-offs 5
3.2 Full field at arbitrary position 6
3.3 Calculation of the mid-plane field derivatives 6

4 Acceleration in a 150 MeV proton FFAG ring **8**
4.1 First order data 8
4.2 Large amplitude transverse motion 10
4.3 Synchrotron motion 10

5 Comments **11**

Appendix **13**

A The "`DIPOLE`" procedure **13**

B 3-D field map versus geometrical model **13**

C Sharp edge field model **14**

1 Introduction

Fixed field alternating gradient (FFAG) accelerators science is subject to a regain of interest [1] in the context of muon acceleration for the neutrino factory [2], with as an outcome investigation of possible application in various domains as hadrontherapy and other high power accelerators [3].

Stepwise ray-tracing is considered (from the very beginning [4]) a good technique to track particles in FFAG's, allowing to draw machine parameters from single- or multi-turn tracking. The developments presented here are based on such methods using the ray-tracing code Zgoubi [5].

A strong concern that motivates these software developments is in simulating in a correct manner the field in the FFAG magnets. This has various aims, as : offering tools for fast optimization of magnet geometry and fields as constrained by accelerator design parameters ; providing correct simulation of multiturn motion in FFAG, with such outcomes as the right computation of lattice parameters as tunes, tune variations, time of flight, etc. ; yielding precision 6-D multiturn tracking and motion stability limits.

In addition, the present developments can be applied to various other magnetic devices involved in manipulation of the large emittance muon beam in the neutrino factory, as for instance compression chicanes [6], muon beam cooling rings [7], with the potential of magnet/field parameters adjustments thanks to the built-in Zgoubi fitting procedure, whereas optimizations based on 3-D magnet code calculations strongly lack flexibility in that matter.

In the following, Section 2 first recalls the principles of the Zgoubi method relevant to the simulation of large acceptance dipoles, Section 3 describes the method for simulating dipole N-uplets, possibly featuring strong radial non-linearity, and the particular case of FFAG magnets, with illustration by a radial-sector FFAG triplet, Section (4) shows a simulation of the KEK 150 MeV proton ring that is based on an FFAG triplet cell.

2 The ray-tracing method, ingredients

We first recall the ingredients of the Zgoubi method that intervene in the implementation of dipole N-uplet simulations.

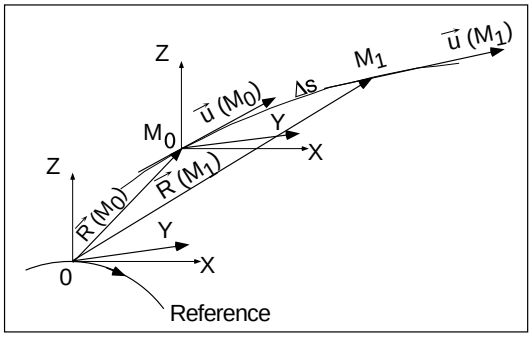

Figure 1: Zgoubi frame and coordinates.

Position and velocity

The integration method is based on stepwise resolution of Lorentz equation by a technique of Taylor series. The working frame is shown in Fig. 1.

Position and velocity of a particle subject to $m d\vec{v}/dt = q\,\vec{v} \times \vec{b}$ are tracked using truncated Taylor expansions in the integration step Δs

$$\begin{aligned} \vec{R}(M_1) &\approx \vec{R}(M_0) + \vec{u}(M_0)\,\Delta s + \vec{u}'(M_0)\,\tfrac{\Delta s^2}{2!} + ... + \vec{u}'''''(M_0)\,\tfrac{\Delta s^6}{6!} \\ \vec{u}(M_1) &\approx \vec{u}(M_0) + \vec{u}'(M_0)\,\Delta s + \vec{u}''(M_0)\,\tfrac{\Delta s^2}{2!} + ... + \vec{u}'''''(M_0)\,\tfrac{\Delta s^5}{5!} \end{aligned} \qquad (1)$$

wherein $\vec{u} = \vec{v}/v,\ \Delta s = v\,\Delta t,\ \vec{u}' = d\vec{u}/ds,\ m\vec{v} = mv\vec{u} = q\,B\rho\,\vec{u}$, and with the derivatives $\vec{u}^{(n)} = d^n\vec{u}/ds^n$ given by $\vec{u}' = \vec{u} \times \vec{B},\ \vec{u}'' = \vec{u}' \times \vec{B} + \vec{u} \times \vec{B}',\ \vec{u}''' = \vec{u}'' \times \vec{B} + 2\vec{u}' \times \vec{B}' + \vec{u} \times \vec{B}''$, etc.

Taylor coefficients

Computation of the coefficients in Eqs. 1 requires the knowledge of the magnetic field $\vec{B}(s)$ and derivatives $d^n\vec{B}/ds^n \quad (n \leq 5)$ in the orthogonal frame (O,X,Y,Z) (Fig. 1). On the other hand, the magnetic field in a dipole can be obtained from a mid-plane model of the vertical field component (the horizontal component is

zero by symmetry), in cylindrical coordinates, of the form $B_z(r,\theta) = B_{z0}\,\mathcal{F}(r,\theta)\,\mathcal{R}(r)$, with factors $\mathcal{F}(r,\theta)$ and $\mathcal{R}(r)$ accounting for the longitudinal (e.g., field fall-offs at dipoles' ends) and for the transverse (e.g., transverse non-linearities) variation of the dipole field. The way the mid-plane field and its derivatives

$$B_z(r,\theta), \qquad \frac{\partial^{k+l} B_z}{\partial\theta^k \partial r^l} \tag{2}$$

at all (r,θ) are obtained from this model is detailed in Section 3.

Once this is done, a transformation from the cylindrical frame of the magnet into the Cartesian frame in Fig. 1 is performed using

$$\frac{\partial B_z}{\partial X} = \frac{1}{r}\frac{\partial B_z}{\partial\theta},\ \frac{\partial B_z}{\partial Y} = \frac{\partial B_z}{\partial r},\ \frac{\partial^2 B_z}{\partial X^2} = \frac{1}{r^2}\frac{\partial^2 B_z}{\partial\theta^2} + \frac{1}{r}\frac{\partial B_z}{\partial r},\ \frac{\partial^2 B_z}{\partial X\partial Y} = \frac{1}{r}\frac{\partial^2 B_z}{\partial\theta\partial r} - \frac{1}{r^2}\frac{\partial B_z}{\partial\theta},\ \text{etc.}$$

Next, Z-derivatives and extrapolation off mid-plane are obtained from Maxwell equations and Taylor expansions, thus yielding the 3-D field description

$$\vec{B}(X,Y,Z), \qquad \frac{\partial^{k+l+m}\vec{B}}{\partial X^k \partial Y^l \partial Z^m}$$

Eventually, $\vec{B}(s)$ and $d^n\vec{B}/ds^n$ needed in Eqs. 1 are derived using the transformations

$$\vec{B}'(s) = \sum_i \frac{\partial\vec{B}(X,Y,Z)}{\partial X_i}\,u_i(s)\ , \qquad \vec{B}''(s) = \sum_{ij}\frac{\partial^2\vec{B}(X,Y,Z)}{\partial X_i\partial X_j}\,u_i(s)\,u_j(s) + \sum_i \frac{\partial\vec{B}(X,Y,Z)}{\partial X_i}\,u_i'(s) \quad etc.$$

wherein the $X_{i,j,\ldots(\,i,j,\ldots=1-3)}$ stand for $X,\ Y$ or Z.

3 An N-uplet magnet procedure. FFAG magnet

This Section describes the way the vertical field component $B_z(r,\theta)$ and derivatives (Eq. 2) at all position in the median plane of a magnet composed of N neighboring dipoles with overlapping fields are calculated.

The method is derived from an existing procedure, "`DIPOLE`", generally used for the design of large acceptance spectrometers (see Appendix for details), and will yield two new procedures named respectively "`DIPOLES`" and "`FFAG`", that mostly differ by the radial dependence of the magnetic field and of the magnet gap as described below. Principles of the "`DIPOLE`" method are recalled in Fig. 2 : a reference radius RM and a reference angle ACN together with angles $\omega^{\pm}$ serve for the positioning of the *ENTRANCE*, *EXIT* and possibly *LATERAL EFBs*. These can be more or less curved (using the R_1, R_2, u_1, u_2 parameters) and given a wedge angle (the θ parameters). The total sector angle AT of the field extent accounts for the fringe field regions at both ends.

Now, let us write the magnetic field at all (r,θ) in the median plane ($z=0$) due a single one (index i) of the dipoles of a N-uplet magnet under the form

$$B_{zi}(r,\theta) = B_{z0,i}\,\mathcal{F}_i(r,\theta)\,\mathcal{R}_i(r) \tag{3}$$

wherein $B_{z0,i}$ is a reference field. The factor $\mathcal{R}_i(r)$ models the r dependence of the field. In the case of the "`DIPOLES`" procedure $\mathcal{R}_i(r)$ is a regular expansion of the form

$$\mathcal{R}_i(r) = b_{0_i} + b_{1_i}(r - R_{0,i})/R_{0,i} + b_{2_i}(r - R_{0,i})^2/R_{0,i}^2 + \ldots \tag{4}$$

proper to simulate for instance chicane dipoles [6], isochronous [8] or superconducting [9] FFAG magnets, whereas in the case of the "`FFAG`" procedure it writes

$$\mathcal{R}_i(r) = (r/R_{0,i})^{K_i} \tag{5}$$

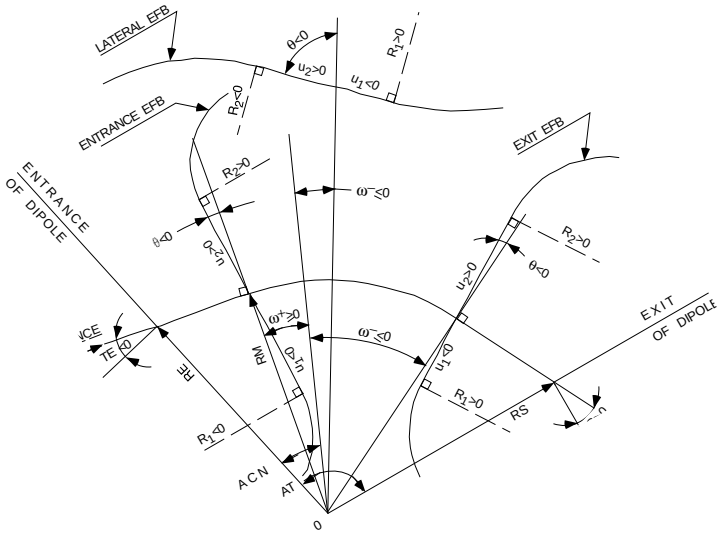

Figure 2: Description of the geometry of a single dipole.

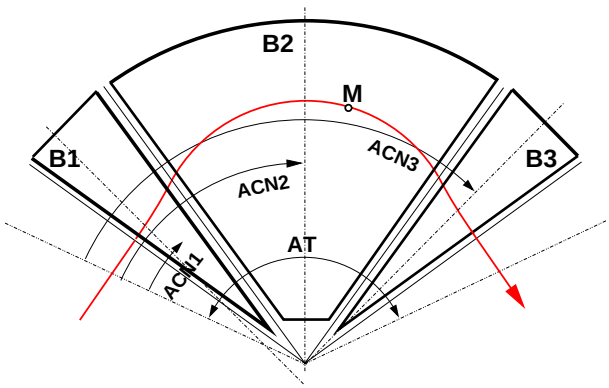

Figure 3: Definition of a dipole triplet using "`DIPOLES`" or "`FFAG`" procedure.

with $R_{0,i}$ being a reference radius and $B_{z0,i}$ the field at $R_{0,i}$ (see Fig. 3), and K being the field index. The factor $\mathcal{F}_i(r,\theta)$ models the azimuthal dependence of the field. In the present work we will not address the spiral-sector case and will restrict the role of $\mathcal{F}_i(r,\theta)$ to simulating the field fall-offs (fringe fields) at *EFBs*, and the field variation in the intermediate region between two neighboring dipoles, in the way described hereafter.

3.1 Field fall-offs

The field fall-off (Fig. 4) at a particular *EFB* (e.g., *Entrance*, *Exit EFB*, see Fig. 2) is modeled by [10, p. 240]

$$\begin{aligned} \mathcal{F}_{EFB}(d) &= 1 \,/\, (1+\exp[p(d)]) \,, \\ p(d) &= C_0 + C_1 d/g + C_2 (d/g)^2 + \ \dots \ + C_5 (d/g)^5 \end{aligned}$$

wherein d is the distance to that *EFB* and depends on r and θ (Fig. 5), and the normalizing coefficient g is normally homogeneous to the gap and can be a function of r, see below. The numerical coefficients $C_0 - C_5$ may be determined from prior matching with realistic fringe field data.

An adequate positioning of the *EFB* makes possible to satisfy (referring to the frame as defined in Fig. 4)

$$\int_{d=-\infty}^{0} \mathcal{F}_{EFB}(u)\, du = \int_{d=0}^{\infty} (1 - \mathcal{F}_{EFB}(u))\, du$$

which entails that varying g will not change the magnetic length, it will just change the fall-off steepness.

A convenient consequence of this is that g can be made dependent of r as for instance in the case of pole shaping

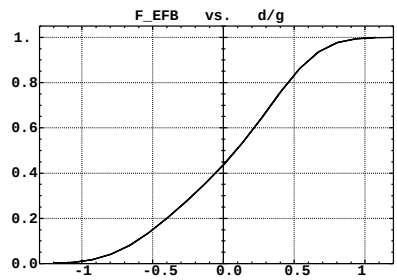

Figure 4: Typical fringe field $\mathcal{F}_{EFB}(d/g)$.

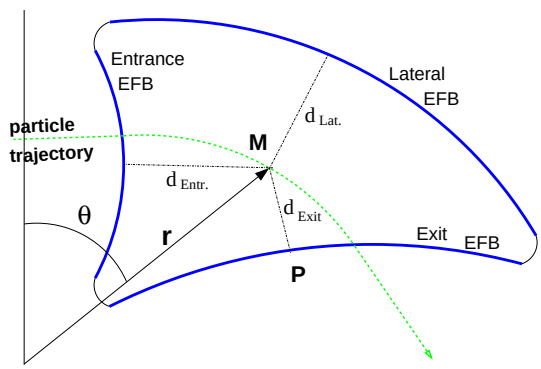

Figure 5: Ingredients in computation of fringe field form factors.

FFAG magnets whose gap satisfies

$$g(r) = g_0(R_0/r)^{\kappa} \qquad (6)$$

with normally $\kappa \approx K$. Each one of the three possible *EFBs* (Figs. 2 and 5) has its own fringe field factor, $\mathcal{F}_{\text{Entrance}}$, $\mathcal{F}_{\text{Exit}}$, $\mathcal{F}_{\text{Lateral}}$. The resulting form factor at particle position (r, θ) due to dipole (i) of the N-uplet is thus taken to be

$$\mathcal{F}_i(r,\theta) = \mathcal{F}_{\text{Entrance}}(r,\theta) \times \mathcal{F}_{\text{Exit}}(r,\theta) \times \mathcal{F}_{\text{Lateral}}(r,\theta) \qquad (7)$$

3.2 Full field at arbitrary position

Now, accounting for N neighboring dipoles in an N-uplet, the mid-plane field and field derivatives are obtained by addition of the contributions of the N dipoles taken separately, namely

$$B_z(r,\theta) = \sum_{i=1,N} B_{zi}(r,\theta) = \sum_{i=1,N} B_{z0,i}\,\mathcal{F}_i(r,\theta)\,\mathcal{R}_i(r) \ , \quad \frac{\partial^{k+l}\vec{B}_z(r,\theta)}{\partial\theta^k\partial r^l} = \sum_{i=1,N} \frac{\partial^{k+l}\vec{B}_{zi}(r,\theta)}{\partial\theta^k\partial r^l} \qquad (8)$$

with $\mathcal{R}_i(r)$ being defined by either Eq. 4 or Eq. 5. Note that, in doing so it is not meant that field superposition does apply in reality, it is just meant to provide the possibility of obtaining a realistic field shape, that would for instance closely match (using adequate $C_0 - C_5$ sets of coefficients) 3-D field simulations obtained from magnet codes.

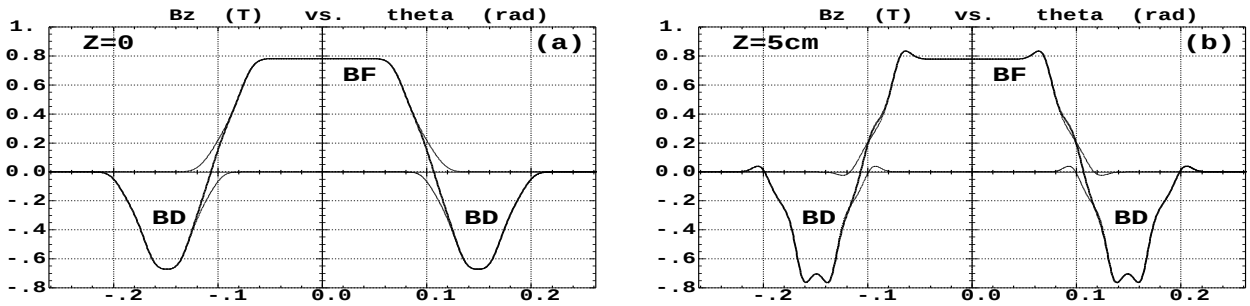

Figure 6: Typical magnetic field $B_z(r_0, \theta, z)$ (Eq. 8) as observed at traversal of the 30 degree sector FFAG triplet for $r_0 = 4.87$ m (the 50 MeV closed orbit region) and for either, **(a)** : $z = 0$ or, **(b)** : $z = 5$ cm as obtained by off mid-plane extrapolation. On both plots the solid curve represents the full field, as obtained by superposition of the separate contributions of each one of the three dipoles represented by the dashed curves.

Eventually, the 6-D field model $\vec{B}(r,\theta,z)$ and derivatives $\partial^{k+l+m}\vec{B}/\partial r^k\partial\theta^l\partial z^m$ are deduced by z-extrapolation accounting for Maxwell equations (see Sec. 2).

This procedure is illustrated in Fig. 6 in the case of an FFAG triplet with characteristics drawn from the KEK 150 MeV proton machine [11], with field fall-offs as in Fig. 4 and $g(r)$ given by Eq. 6.

3.3 Calculation of the mid-plane field derivatives

Two methods have been implemented to calculate the field derivatives in the median plane (Eq. 8), based on either analytical expressions related to the magnet geometry or classical numerical interpolation.

The first method has the merit of insuring best symplecticity in principle and fastest tracking.

The interest of the second method is in its facilitating possible changes in the mid-plane magnetic field model $B_z(r,\theta)$, for instance if simulations of shims, defects, or special r, θ field dependence need to be introduced.

Analytical formulation The analytical formulations of the field derivatives in Eq. 8 to be fed into the source Fortran have been obtained using *Mathematica*. The starting ingredients are, on the one hand distances to the *EFBs* (Fig. 5), $d(r,\theta) = \sqrt{(x(r,\theta) - x_0(r,\theta))^2 + (y(r,\theta) - y_0(r,\theta))^2}$ to be computed for all three cases, d_{Entrance}, d_{Exit}, d_{Lateral}, on the other hand the expressions of the coordinates of particle position M and its projection P on the *EFB* in terms of the magnet geometrical parameters

$$\begin{aligned}
x(r,\theta) &= \cos(ACN - \theta) - R_0 \\
y(r,\theta) &= r\sin(ACN - \theta) \\
x_P(r,\theta) &= \sin(u)\ (y(r,\theta) - y_b)/2 + x_b\ \sin^2(u) + x(r,\theta)\ \cos^2(u) \\
y_P(r,\theta) &= \sin(u)\ (x(r,\theta) - x_b)/2 + y_b\ \cos^2(u) + y(r,\theta)\ \sin^2(u)
\end{aligned}$$

with $x_b,\ y_b,\ u$ parameters drawn from the magnet geometry (sector angle, wedge angle, face curvatures, etc.). These ingredients allow calculating the derivatives $\frac{\partial^{u+v}x(r,\theta)}{\partial\theta^u\partial r^v}$, $\frac{\partial^{u+v}y(r,\theta)}{\partial\theta^u\partial r^v}$, $\frac{\partial^{u+v}x_0(r,\theta)}{\partial\theta^u\partial r^v}$, $\frac{\partial^{u+v}y_0(r,\theta)}{\partial\theta^u\partial r^v}$. which in turn which intervene the derivatives of the compound functions $\frac{\partial^{u+v}F(r,\theta)}{\partial\theta^u\partial r^v}$, $\frac{\partial^{u+v}p(r,\theta)}{\partial\theta^u\partial r^v}$, $\frac{\partial^{u+v}d(r,\theta)}{\partial\theta^u\partial r^v}$.

Numerical interpolation The expression $B_z(r,\theta)$ in Eq. 8 is computed at the $n \times n$ nodes ($n = 3$ or 5 in practice) of a "flying" interpolation grid in the median plane centered on the projection m_0 of the actual particle position M_0 as schemed in Fig. 7. A polynomial interpolation is involved, of the form $B_z(r,\theta) = A_{00}+A_{10}\theta+A_{01}r+A_{20}\theta^2+A_{11}\theta r+A_{02}r^2$ that yields the requested derivatives, using $A_{kl} = \frac{1}{k!l!}\frac{\partial^{k+l}B}{\partial\theta^k\partial r^l}$. Note that, the source code contains the explicit analytical expressions of the coefficients A_{kl} solutions of the normal equations, so that the operation is not so CPU time consuming.

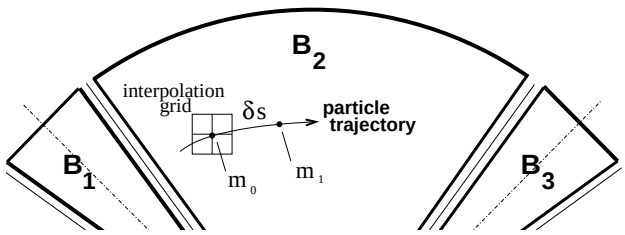

Figure 7: Interpolation method. m_0 and m_1 are the projections in the median plane of particle positions M_0 and M_1 (see Fig. 1) separated by one integration step Δs.

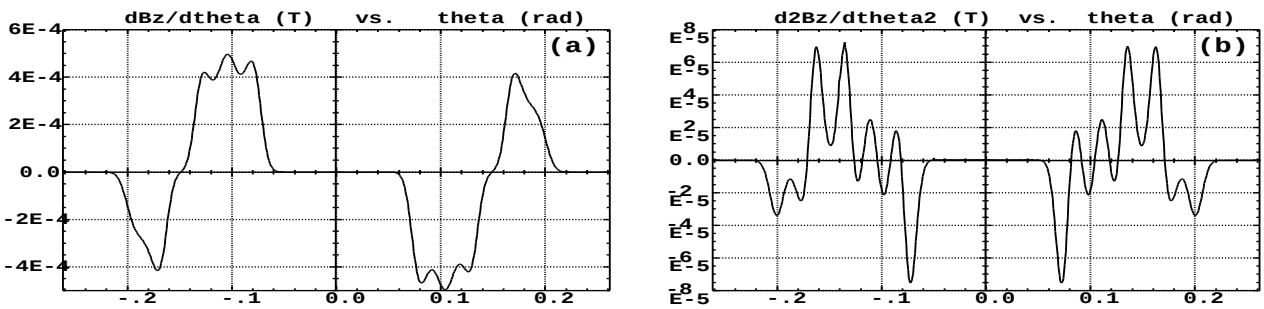

Figure 8: Field derivatives at traversal of the FFAG sector triplet at constant radius, after Eq. 8. **(a)** : $\partial B_z(r,\theta)/\partial\theta$, **(b)** : $\partial^2 B_z(r,\theta)/\partial\theta^2$.

Typical shapes of the derivatives so obtained are displayed in Fig. 8. Note that, their rapid variation with θ indicate that accordingly small integrations step size (Δs in Eq. 1) should be employed. In addition, when using the numerical interpolation method (Fig. 7), a small enough mesh size should be used [1].

[1]The same remark holds as to using dense mesh when tracking through magnetic field maps, as pointed out in Ref. [14].

4 Acceleration in a 150 MeV proton FFAG ring

The goal here is to show that these simulations provide the right results. For that purpose the geometrical model is submitted to various numerical experiments,

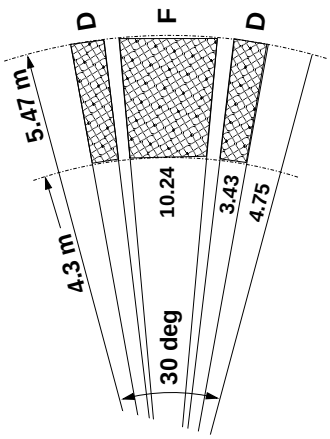

Figure 9: 150 MeV DFD triplet.

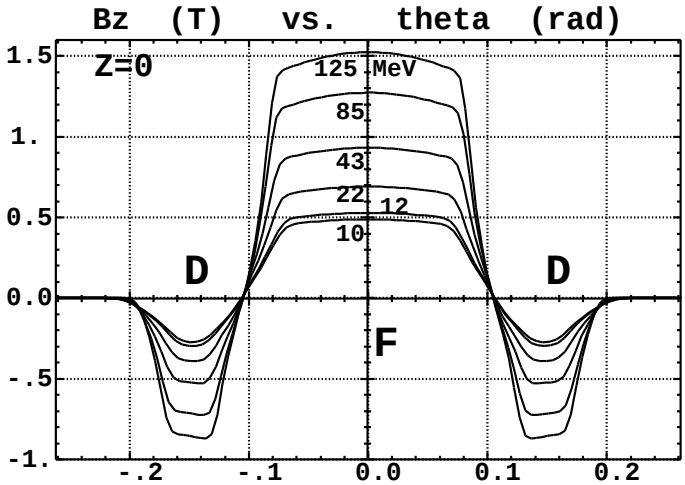

Figure 10: Field along various closed orbits in a cell of the 150 MeV proton FFAG addressed in Section 4.

A 12-cell machine is considered, representative of the KEK 150 MeV FFAG [11, 12]. The cell is a 30 degree sector DFD (Fig. 9). Its design parameters are as follows : reference radius $R_0 = 5.4$ m and $K = 7.6$ (in Eq. 5), gap shape determined by $\kappa = 3$ (in Eq. 6), field fall-offs as in Fig. 4. This yields field along closed orbits as schemed in Fig. 10, no too far from computed 3-D field maps representative of the actual magnets, this is discussed in App. B. As a consequence the working tunes are close to those considered in Ref. [14], which one can refer to for detailed comparisons with 3-D field map tracking results.

4.1 First order data

Fig. 11 shows the closed orbits in a cell at various energies, Fig. 12 gives sample beam envelopes for $\epsilon_{r,z}/\pi = 200$ mm.mrad. Betatron functions can be drawn from this type of output using paraxial rays, sample values at the center of the drift are displayed in Fig. 13.

Total tunes (12 cell ring) are given in Fig. 14 ; the way their integer part has been obtained is described below. It can be observed that the horizontal tune is constant as can be expected from the zero-chromaticity conditions resulting from the r^K dependence of the magnetic field ; on the other hand the vertical chromaticity is not zero, which is attributed to the field fall-offs, *i.e.*, the azimuthal variation of the field in our geometrical model is not quite independent of radius - in contrast, a sharp edge field model yields zero chromaticities and constant values $\nu_r = 3.773$, $\nu_z = 1.574$, this is discussed in App. C.

The momentum compaction $\alpha = d\mathcal{L}/\mathcal{L} \,/\, dp/p$ is computed from Δp induced difference in closed orbit lengths, sample values are given in Tab. 1 and fairly satisfy the theoretical relation $\alpha \approx 1/(1+K)$ given $K = 7.6$.

All these results demonstrate very good consistency on the one hand with theoretical data, and on the other hand with published material [11, 12, 14].

Note : The integer part of the tunes in Fig. 14 has been calculated as follows. We note $\beta(s) = \overline{\beta} + \delta\beta(s)$ with $\overline{\beta} = \int_{cell} \beta(s)ds \,/\, \mathcal{L}_{cell}$ the average beta value over a cell so that $\int_{cell} \delta\beta(s)ds = 0$, and $\mathcal{L}_{cell} = \mathcal{L}/12$.

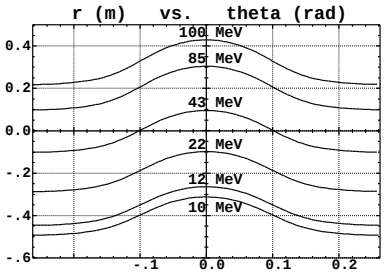

Figure 11: Closed orbits in the DFD cell at various energies.

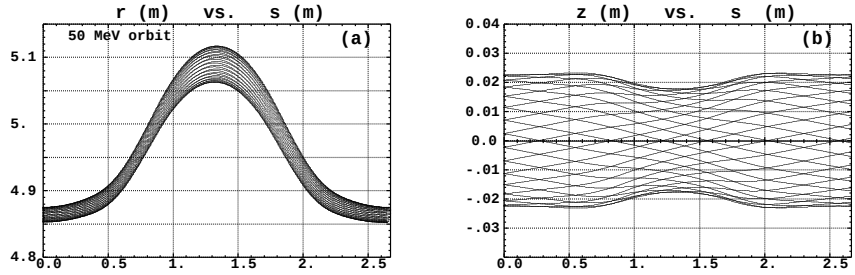

Figure 12: Horizontal **(a)** and vertical **(b)** beam envelopes in a cell for respectively $\epsilon_r/\pi = 200$ mm.mrad and $\epsilon_z/\pi = 200$ mm.mrad.

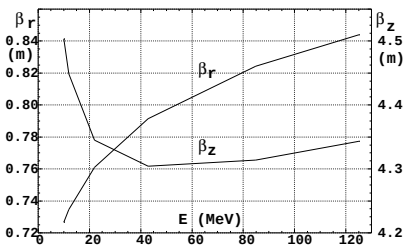

Figure 13: Betatron function values at center of drift.

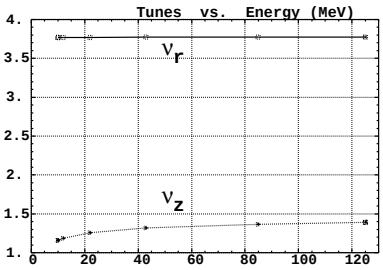

Figure 14: Machine tunes.

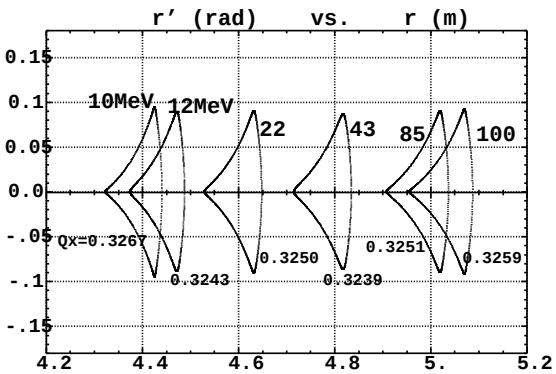

Figure 15: Horizontal phase space, the limits of stable motion (accuracy better than $\Delta r = \pm 0.1$ mm) for 5 energies.

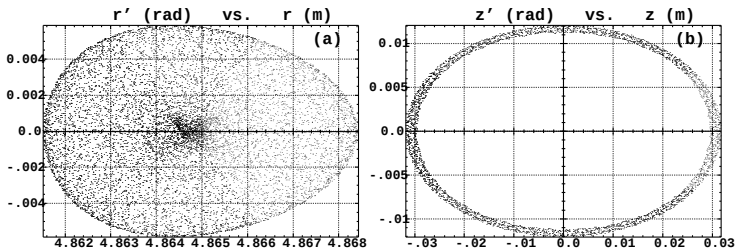

Figure 16: Horizontal **(a)** and vertical phase space **(b)**, for a particle launched on 50 MeV horizontal closed orbit with non-zero z-motion.

We assume that the beta functions are smooth enough that $1/\beta(s) \approx (1-\delta\beta(s)/\overline{\beta})/\overline{\beta}$. That yields $\overline{\left(\frac{1}{\beta}\right)} \approx \frac{1}{\overline{\beta}} - \frac{1}{\mathcal{L}_{cell}\overline{\beta}^2}\int_{cell}\delta\beta(s)ds = \frac{1}{\overline{\beta}}$ so that cell tunes satisfy $\nu_{r,z_{cell}} = \frac{1}{2\pi}\int_{cell}\frac{ds}{\beta(s)} = \frac{\mathcal{L}_{cell}}{2\pi}\overline{\left(\frac{1}{\beta}\right)} = \frac{\mathcal{L}_{cell}}{2\pi\overline{\beta}}$. On the other hand, numerical results (or grossly, the square root of the mean value of the envelopes in Fig. 12) show that $\mathcal{L}_{cell}/\overline{\beta_r} \approx 2.5$ and $\mathcal{L}_{cell}/\overline{\beta_z} \approx 1/2$, so that both cell tunes have zero integer part, and full tunes are just 12 times the fractional cell-tune values as delivered for instance by multiturn Fourier analysis.

4.2 Large amplitude transverse motion

Fig. 15 shows horizontal phase space trajectories at the limit of stable motion in the ring, as observed at center of a drift, together with the related fractional tunes whose values differ from first order ones (Fig. 14) due to amplitude detuning induced by the non-linear field ; the triangle shape of phase space motion is related to the presence of strong sextupole component in $B(r)$ (Eq. 5) and the proximity to third integer tune. Fig. 16 shows phase space motion at 50 MeV, observed at center of drift ; the horizontal motion clearly shows non-linear $r-z$ coupling induced horizontal motion, given that the particle was launched on closed orbit ($r_0 = r_{c.o.,\ 50\ MeV}$, $r'_0 = 0$). The horizontal symplecticity is very good, up to separatrix regions (Fig. 15) ; it is to be determined whether the vertical motion spreading in Fig. 16-right is effectively free of non-symplecticity effects, although a good indication is that the motion stays confined within the finite limits actually displayed in both r and z phase-spaces.

Another feature revealed in Fig. 15 is the large geometrical acceptance characteristic of FFAG optics : the surface of the 10 MeV stability limit portrait is $\epsilon_x = 1$ cm about, 2.5 times the nominal emittance practiced at the KEK 150 MeV FFAG [11].

4.3 Synchrotron motion

Peak RF voltage $\hat{V} = 19$ kV is considered here, a value somewhat larger than that used at KEK [12], for the sake of faster tracking.

Table 1: Parameters of longitudinal motion. (num. : numerical values, from tracking ; th. : theoretical values from formulas in the text).

E (MeV)	orbit length $\mathcal{L}$ (m)	f_{rev} (MHz)	α	ν_s	bucket height $\pm\Delta p/p$ (%)
	num.	num.	num.$^{(a)}$	num. / th.	num. & th.$^{(b)}$
10	28.6333	1.516522	0.11605	0.011325 / 0.011451	2.654
22	29.9794	2.124539	0.11611	0.007593 / 0.007649	1.824
43	31.1885	2.808931	0.11616	0.005339 / 0.005367	1.344
125	33.2724	4.238662	0.11619	0.002909 / 0.002917	0.881

(a) The theoretical value is $\alpha = 1/(1+K) = 0.11628$.
(b) The agreement is better than 10^{-4}, relative.

Stationary bucket dynamics is investigated first, as illustrated in Fig. 17.

Complete tracking results are given in Tab. 1, they are in excellent agreement with theoretical data, also given in Tab. 1, as drawn from :
- phase slippage factor $\eta = \frac{1}{\gamma^2} - \alpha = \frac{1}{\gamma^2} - \frac{1}{1+K}$ and taking $K = 7.6$,
- synchrotron frequency : $f_s = \Omega_s/2\pi = \frac{c}{\mathcal{L}}\left(\frac{h\eta\cos\phi_s q\hat{V}}{2\pi E_s}\right)^{1/2}$, given $h = 1$, $\phi_s = 0$, $q\hat{V} = 19$ keV ; E_s is the synchronous energy, $\mathcal{L}$ and T_{rev} are obtained by tracking (Tab. 1),

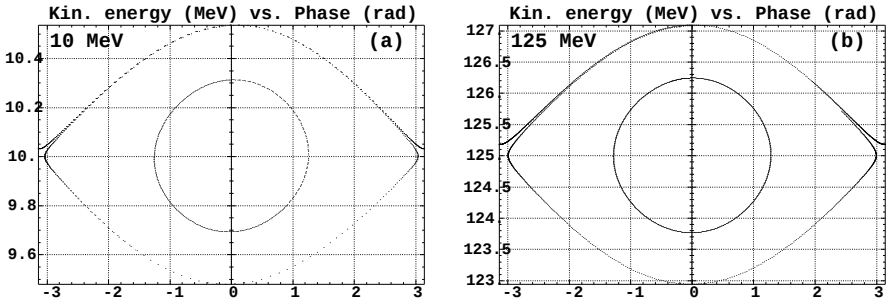

Figure 17: Stationary buckets in the **(a)** 10 MeV and **(b)** 125 MeV regions.

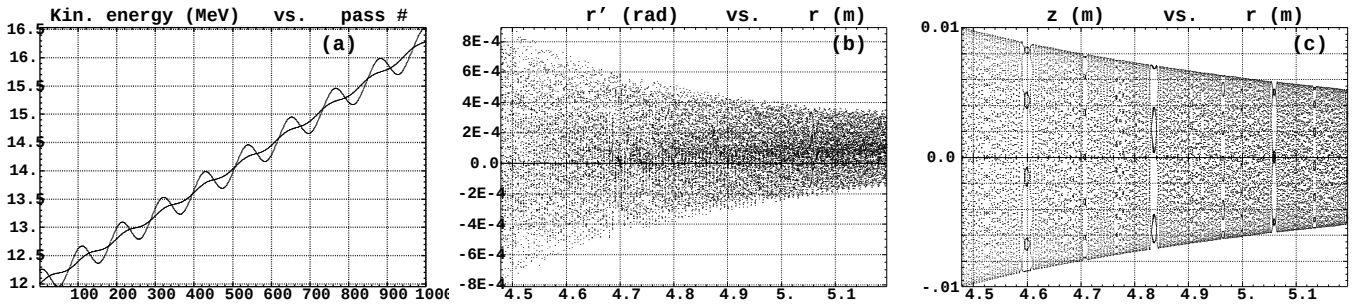

Figure 18: Acceleration cycle. **(a)** : two motions close synchronous particle. **(b)** and **(c)** : respectively, horizontal motion over the full cycle, 20000 turns, from 12 to 150 MeV, and the corresponding vertical motion.

- synchrotron tune : $\nu_s = f_s \times T_{rev}$,
- bucket height $\pm\frac{\Delta p}{p} = \pm\frac{1}{\beta_s}\left(\frac{2q\hat{V}}{\pi h \eta E_s}\right)^{1/2}$.

A full acceleration cycle, from 12 to 150 MeV is experimented next.

The RF is increased *linearly with turn number* (this RF program is purely arbitrary) from 1.62 to 4.63 MHz, synchronous phase $\phi_s = 20$ degrees which means about $2\,10^4$ turns to complete the cycle.

Sample tracking results are displayed in Fig. 18 and show excellent behavior. A $\Delta s = 1$ mm integration step size has been taken, sensibly smaller than the oscillation frequency of the second order derivatives (Fig. 8) so to insure enough sufficient precision in computation of Eqs. 1.

It can be observed that the vertical motion undergoes regular damping, $(B\rho_{12\,\mathrm{MeV}}/B\rho_{150\,\mathrm{MeV}})^{1/2} \approx 0.52$ from start to end of the cycle ; the radial motion does not satisfy that, however it is of extremely low amplitude in the vicinity of the closed orbit and may be subject to coupling effects due to the z motion, as already pointed out concerning Fig. 16.

5 Comments

Using the analytical derivatives method allows fast tracking, with high accuracy, and makes the code a powerful tool for long term tracking, DA tracking, transmission efficiency calculations (a strong concern in capture/acceleration of unstable particle beams), etc. Numerical interpolation of the field from mid-plane field model instead (Figs. 6, 10), is also efficient, it has the merit of allowing the field model to be changed easily (it is just a matter of changing the mid-plane field model, Eq. 3) and yields very good accuracy as well, but computing speed lower by a factor of slightly more than 2.

Accounting for the built-in fitting procedure, these developments make Zgoubi an efficient tool for FFAG optics and machine design studies. The code has at present been used with success for design studies, DA tracking and various validations concerning linear non-scaling optics (acceleration of muons) [20], non-linear non-scaling FFAG optics (protontherapy application) [21] and an isochronous cell (acceleration of muons, electron-model of non-scaling FFAG) [22].

It is planned to compare the magnetic fields (Fig. 10) as obtained with the method described in this paper, and the ensuing tracking results, with 3-D magnet calculations and tracking in field maps, as addressed in App. B. Works have already been tackled on that topic and will be pursued [14].

CPU time - Computing speed tests were performed upon 12 to 150 MeV acceleration in the 12 cell FFAG ring (conditions as in Fig. 18), using two different processors, Pentium III 1 GHz or Xeon 2.8 GHz, under Linux system. Derivatives are computed with either the analytical or the numerical method, up to either second or fourth order as indicated in the Table below, whereas an integration step size $\Delta s = 0.5$ cm is considered so to insure convergence of the numerical integration in any of these cases.

CPU time (seconds per turn per particle) :

	Pentium III 1 GHz		Xeon 2.8 GHz	
	Analyt.	Num.	Analyt.	Num.
2nd order	0.17 s	0.40 s	0.10 s	0.25 s
4th order	0.44 s	1.00 s	0.17 s	0.64 s

Such computing speed means that one can envisage overnight runs on computer network systems, aiming at such goals as long-term DA tracking, 6-D multi-turn beam transmission, resonance crossing studies.

Appendix

A The "DIPOLE" procedure

The Figure shows the iso-field regions in the median plane of the large acceptance Elbeck spectrometer SPES3 once operated at SATURNE for rare decay experiments (typically, 3.4 T.m rigidity) [15, 16]. That field model had been obtained using the "DIPOLE" procedure whereas magnet edges and corresponding field fall-offs where optimized using POISSON and matched for "DIPOLE" purpose as described in Section 3.1.

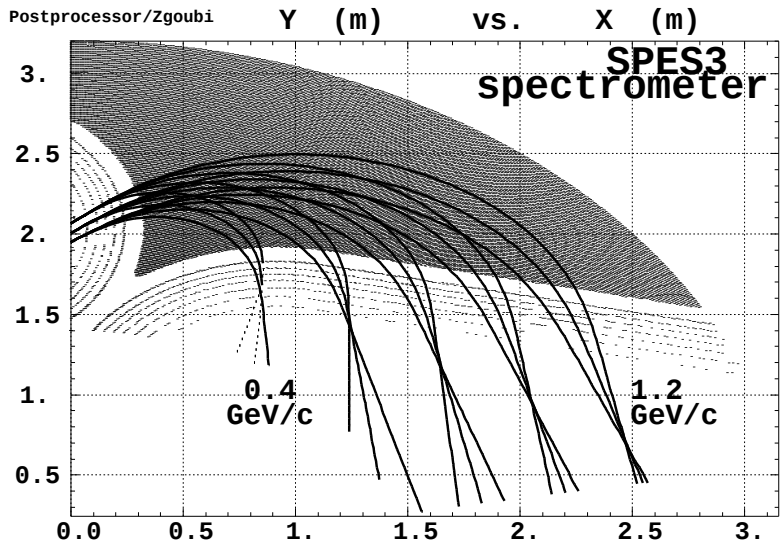

The same method has been used to design several other spectrometers as SPES2 [17, 16], SPEG at GANIL [18], the 1.8 GeV Kaon QD spectrometer at GSI [19].

B 3-D field map versus geometrical model

In the main text, a 3-dipole representation of the 150 MeV FFAG sector magnet is involved Fig. 9. However, a characteristic feature of the actual magnet is in its non-zero fringe field over the drift (Fig. 19-a), about 700 Gauss independent of the radius. This feature can be reproduced using 5 dipoles with the "FFAG" procedure as schemed in Fig. 19-b,c instead of just 3 as in Fig. 9.

Nevertheless, for the sake of simplicity in the modeling and in numerical demonstration experiments, and in order to stay as close as possible to the theoretical hypothesis, namely $\mathcal{R}_i(r) = (r/R_{0,i})^{K_i}$ and $g(r) = g_0(R_0/r)^{\kappa}$, the the 3-dipole model is used in the present work.

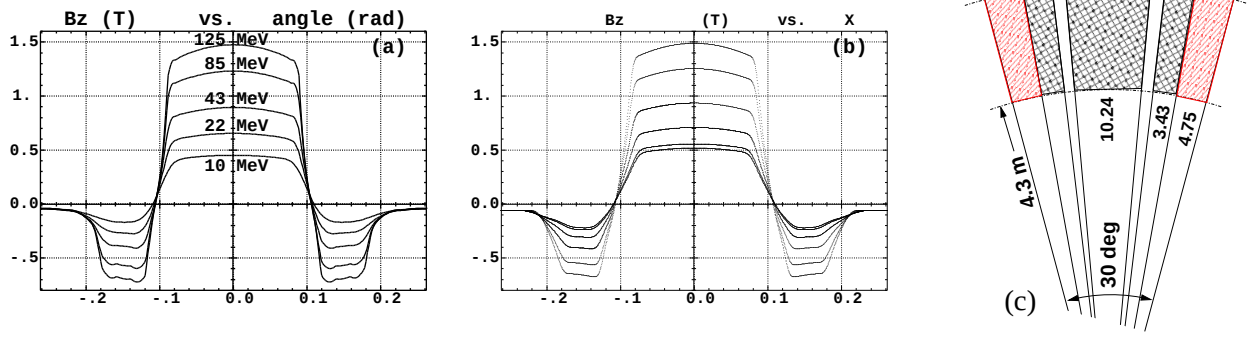

Figure 19: Comparison of magnetic field along closed orbits in the case of, **(a)** : TOSCA 3-D map representative of the KEK 150 MeV FFAG [13, 14] and, **(b)** : a "3+2"-dipole geometrical model. In **(c)** is represented the geometry of the "3+2"-dipole design, involving two regions (hatched) of about 700 G field over the two end drifts.

C Sharp edge field model

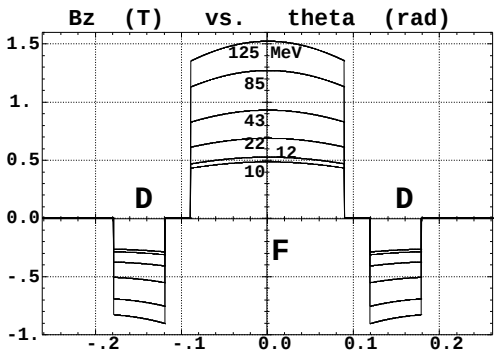

Figure 20: Field on closed orbits, hard edge model.

The geometrical model also allows hard edge fall-offs (Fig. 20). Compared top the soft edge model (field in Fig. 10, closed orbits in Fig. 11) the closed orbit radial positions are but slightly changed, at the millimeter scale.
Tunes have constant values $\nu_r = 3.773$, $\nu_z = 1.574$ over the all energy span as expected from the theory [23], to be compared to soft-edge values in Fig. 14. The horizontal tune is practically independent of the model either hard- or soft-edge, as expected since fringe fields have no effect to first order on horizontal motion. Such is not the case for the vertical motion that shows non-negligible first order effect of fringe fields ($\Delta\nu_z > 0.17$).

References

[1] The rebirth of the FFAG, M. Craddock, CERN Courrier 44-6 (2004).

[2] A feasibility study of a neutrino factory in Japan, KEK report, Feb. 2001.

[3] See for instance, FFAG03 workshop, KEK, Tsukuba, http://hadron.kek.jp/FFAG/FFAG03_HP/index.html.

[4] O CAMELOT ! A Memoir Of The MURA Years (Section 7.1), F.T.Cole, Proc. Cycl. Conf, April 11, 1994.

[5] (a) The ray-tracing code Zgoubi, F. Méot, NIM A 427 (1999) 353-356, and also
(b) Zgoubi users' guide, F. Méot and S. Valero, CEA DAPNIA SEA-97-13 and FERMILAB-TM-2010 (1997).

[6] Magnets for muon front-end chicane, M. R. Harold, Proc. Nufact02 (p. 1679).

[7] Ionization cooling in FFAGs, H. Schonauer, Proc. Nufact02 (p. 1739) ;
FFAG and Weak Focusing Muon Gas-Filled 6-D Cooling Rings, A. Garren, UCLA, H. Kirk and S. Kahn, BNL, FFAG04 Workshop Vancouver, BC, Canada April 15-21, 2004.

[8] Design of an Isochronous FFAG Ring for Acceleration of Muons, G. H. Rees, RAL, UK (private communication).

[9] SC magnets for FFAGs', M. Yoshimoto et als., Proc. NuFact03 Workshop, Columbia Univ., NY (2003).

[10] Deflecting magnets, H.A. Enge, in *Focusing of charged particles*, Vol. 2, A. Septier ed., Academic Press, New-York and London (1967).

[11] A 150 MeV FFAG synchrotron with return-yoke free magnet, T. Adashi et als., Proc. PAC01, Chicago ; Status of 150MeV FFAG synchrotron, S. Machida et als., Proc. PAC03 Conference.

[12] Radio frequency acceleration system for 150MEV FFAG, A. Takagi et als., Proc. PAC03 Conference.

[13] M. Aiba, KEK, private communication, Aug. 2004.

[14] Determination of KEK 150 MeV FFAG parameters from ray-tracing in TOSCA field maps, M. Aiba and F. Méot, CERN-NUFACT-Note-140 (2004). (http://slap.web.cern.ch/slap/NuFact/NuFact/NFNotes.html).

[15] See for instance, Creation of a unique field map for the spectrometer SPES III from measured maps of the focal and fringing fields, W. Rsch et als., CNRS/IN2P3/IPNO-DRE-89-31, Orsay (Sept. 1989).

[16] This spectrometer is now at KEK - private communication by F. Damoy, CEA Saclay.

[17] See for instance, Le spectromètre II, Int^{al} Rep. DPh-N/ME, J. Thirion et P. Birien, CEA Saclay, 23 Dec. 1975.

[18] Spectromètre magnétique à haute résolution pour ions lourds, P. Birien and S. Valero, Report CEA-N-2215, SPhN-ME, CEA Saclay (May 1981).

[19] Calculs optiques pour le spectromètre à kaons de GSI, A. Tkatchenko et F. Méot, CEA/LNS/GT/88-07, Saclay (1988).

[20] Tracking in a 8-16 GeV non-scaling muon FFAG, F. Méot, FFAG03workshop, KEK (2003), http://hadron.kek.jp/FFAG/FFAG03_HP/menu.html.

[21] Design of a non-scaling FFAG accelerator for proton therapy, private communication, D. Trbojevic, FFAG04 workshop, KEK (2004) ;
FFAG Layout for BNL-AGS Upgrade, A. G. Ruggiero, private communication, FFAG04 workshop, KEK (2004).

[22] An isochronous ring for muon acceleration, G.H. Rees, FFAG04 workshop, KEK (2004), http://hadron.kek.jp/FFAG/FFAG04_HP/menu.html.

[23] K. R. Symon, Phys. Rev. 98, 1152A (1955).